The 9th European Congress on Computational Methods in Applied Sciences and Engineering
ECCOMAS Congress 2024
3–7 June 2024, Lisboa, Portugal

A DYNAMIC CT BASED PIPELINE TO ASSESS HEMODYNAMIC INDEXES AND WALL STIFFNESS OF THE AORTA

FRANCESCA DELL'AGNELLO[1,2], EMANUELE VIGNALI[1], KATIA CAPELLINI[1], MARTINO A. SCARPOLINI[1], EMANUELE GASPAROTTI[1], FILIPPO CADEMARTIRI[3] AND SIMONA CELI[1]

[1] BioCardioLab, Bioengineering Unit
Fondazione Toscana Gabriele Monasterio, Massa, Italy
e-mail: fdellagnello@ftgm.it, evignali@ftgm.it. kcapellini@ftgm.it, mascarpolini@ftgm.it, gasparotti@ftgm.it, s.celi@ftgm.it

[2] Department of Information Engineering
University of Pisa, Pisa, Italy

[3] Department of Radiology
Fondazione Toscana Gabriele Monasterio, Pisa, Italy
email: cademartiri@ftgm.it

Key words: Computational fluid dynamics, Mesh morphing, Moving wall, Wall stiffness, Aorta

Summary. Computational Fluid Dynamics (CFD) represents a powerful tool to study blood flow in cardiovascular districts. Commonly, CFD simulations are based on the rigid-wall assumption, which has effects on the hemodynamic results. Instead, Fluid-Structure Interaction simulations are computationally expensive and need additional information concerning vessel wall and thickness. This work aims to develop a new image-based method to set-up moving boundaries CFD simulations ($\mathrm{CFD_{MB}}$) of the entire thoracic aorta (TA). Starting from medical images, we built models of the TA and of the left ventricle (LV) for 20 phases of the cardiac cycle through a custom multi-label 3D U-net. Firstly, the TA 3D models were morphed on the baseline mesh (0%), employing an in-house non rigid registration algorithm. The wall displacement was then used to set-up the $\mathrm{CFD_{MB}}$. Inlet flow conditions extracted from the LV volumes were imposed. Hemodynamic results were compared with those obtained from rigid-wall CFD simulations run on the baseline mesh ($\mathrm{CFD_0}$). For the $\mathrm{CFD_{MB}}$ approach, the shift of the flow waveform was computed and used to estimate the aortic stiffness by applying the principle of the pulse wave velocity. The developed simulation strategy copes with TA morphological changes during the cardiac cycle and highlights differences in hemodynamic parameters, with respect to $\mathrm{CFD_0}$ approach, overcoming the limitations of state-of-the-art simulations.

1 INTRODUCTION

The role of hemodynamics and mechanobiology in the onset and progression of thoracic aorta (TA) pathologies is well-established [1, 2]. The long term interaction between altered blood flow and endothelial cells can result in changes of the arterial wall homeostasis, thus promoting different cardiovascular diseases [3]. The assessment of TA hemodynamics can support clinicians in the diagnosis of TA diseases and in the understanding of the pathophysiology behind TA disease. In this regard, the combined usage of medical images and Computational Fluid Dynamics (CFD) represents a consolidated method to study blood flow patterns and related parameters in a patient-specific manner [4]. However, to successfully translate the use of numerical simulations in the clinical practice low computational times and high accuracy are required. Thus, modelling assumptions and computational set-up have a pivotal role in turning the CFD approach clinically affordable.

Commonly, CFD simulations rely on the rigid-wall assumption to simplify and speed up the numerical approach. However, since the TA undergoes large deformations as a result of the systolic and diastolic loading and unloading associated to the contraction of the left ventricle (LV), such a hypothesis may affect the reliability of the simulation results [5, 6]. Instead, Fluid-Structure Interaction (FSI) method has high computational times and requires the definition of the mechanical behaviour of vessel wall, which is difficult to be achieved from in-vivo data [7]. This lack of information introduces the needing of strong assumptions, such as in terms of the wall thickness and stiffness, thus representing the major source of uncertainties of the FSI approach [5, 8]. Recent studies introduced moving boundary methods (MBM) in the cardiovascular field, also thanks to the current images techniques, particularly electrocardiogram gated computed tomography (ECG-gated CT) images, able to acquire time-resolved anatomies with high resolution [9]. The embedding of CT-based MBM in CFD simulations allow to model the effect of the in-vivo deformations of anatomical structures on the hemodynamics, overcoming the complexity of the FSI approach. In the context of TA, only a few studies are based on MBMs. Capellini et al. [10, 11] embedded the Radial Basis Functions (RBF) mesh morphing technique into CFD simulations to capture the effect of the ascending TA morphological variations on fluid dynamics. Calò et al. [12] applied the just mentioned approach to investigate the impact of ascending TA wall displacement on large-scale flows. Nevertheless, these studies are limited to the ascending region of the TA and showed some intrinsic discontinuities that could not be bypassed considering that the MBM is based on a commercial tool.

The reliability of numerical simulations is also related to boundary conditions. In the TA scenario, the inflow conditions affect hemodynamic parameters [13, 14, 15]. Even if spatial and temporal flow variation are available in case of time-resolved three-dimensional phase-contrast magnetic resonance imaging acquisition, in case of CT scans the spatial information is lacking and simplified plug or parabolic profiles are applied as inlet boundary condition [11, 16, 17]. Indeed, the temporal flow information can be retrieved from ECG-gated CT dataset by calculating the left ventricle volume variation.

This work aims to develop a new CFD environment, fully based on ECG-gated CT images, to set-up moving wall boundaries condition and to apply a patient-specific inlet temporal waveform.

2 MATERIALS AND METHODS

2.1 AI-based image processing

Image acquisition – Images were acquired with a dual source CT scanner using a iodine-containing contrast medium and presented a pixel size of 0.311 x 0.311 mm and a slice thickness of 1 mm. A retrospective ECG-gated protocol was employed. Images were reconstructed at every 5% phase, between two R-R intervals from 0% to 95% (20 phases). CT acquisition was performed on a 43-year-old male subject with a tricuspid aortic valve (TAV) and no evidence of aortic and valvular pathology.

Image segmentation – A custom multi-label 3D U-Net, based on the nnU-Net deep learning framework [18] was employed to automatically extract the labelmaps of the TA and the LV for each acquired phase of the cardiac cycle, as shown in Figure 1. The net was trained on a total of 50 semi-automatically segmented CT scans with a pixel size of 0.571 $\pm$ 0.086 mm and a slice thickness of 0.651 $\pm$ 0.807 mm. CT images were resampled to a voxel size of 1.865 x 1.865 x 0.950 mm and underwent a z-score normalization. Data augmentation, including rotation, scaling, additive gaussian noise, gaussian blur, multiplicative brightness and contrast and mirroring was applied. We employed a combination of equally weighted Dice score and cross-entropy as loss function. Training was performed on anisotropic patches 112 x 224 x 96 with a batch size equal to 2 and run for 1000 epochs.

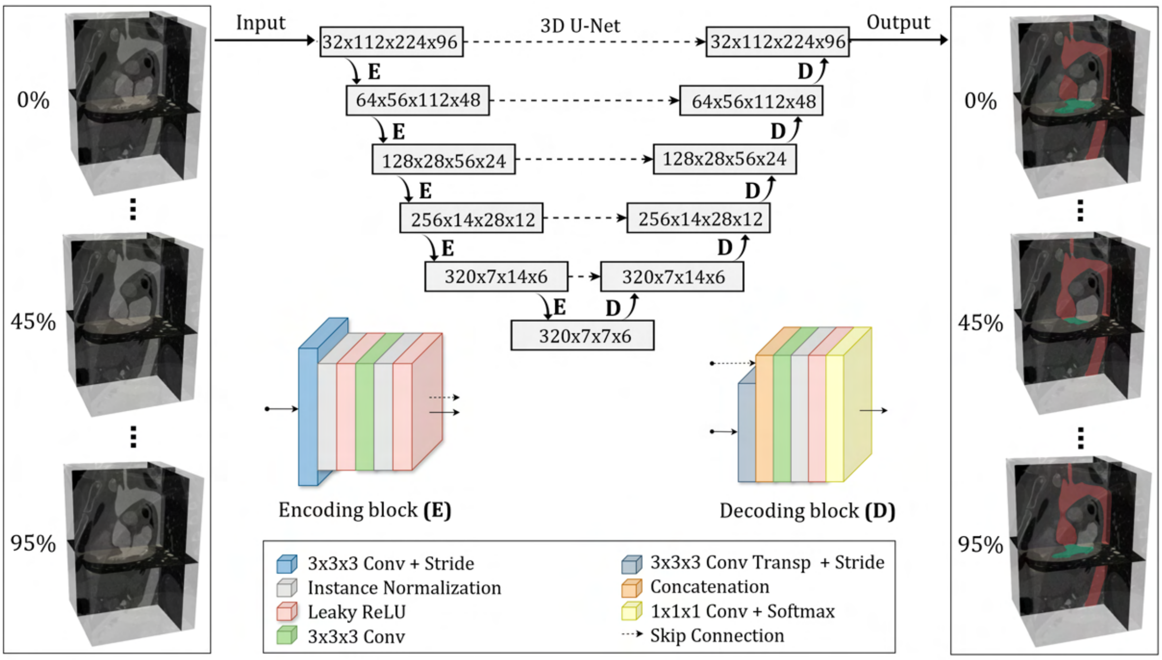

Figure 1: AI-based image segmentation: the 3D U-Net architecture is made up of consecutive encoding blocks and decoding blocks; ECG-gated CT images are used as input; labelmaps of the TA (red) and LV (green) are the outputs.

To evaluate the net performance a stratified K-fold cross-validation (K=5) was performed. We split the entire dataset into equally-numerous and balanced K groups, sorting the data of each fold according to the z-spacing of the original images. For each fold we trained the net on K-1 partitions and used the remaining one as validation set.

3D models creation – Starting from the predicted labelmaps achieved from the 3D U-Net for image segmentation, we reconstructed 3D surface models of the TA and the LV for each phase through a marching cubes algorithm. To remove the common block-like appearance derived from the contours generation a low-pass Taubin surface smoothing filter was applied. Consistently for each phase we clipped the TA geometries at the aortic inlet, descending aorta (DAo) and supra-aortic vessel outlets (brachiocephalic artery (BCA), left common carotid artery (LCCA) and left subclavian artery (LSA)) in a direction orthogonal to the vessel centerline.

2.2 CFD simulations

In this work two types of CFD simulations were performed: i) a rigid wall CFD simulation on the 0% phase model (CFD_0); ii) a moving boundary CFD simulation (CFD_{MB}) based on a mesh morphing technique. To implement the CFD_{MB} and include the actual motion of the TA during the cardiac cycle in the numerical approach we developed a dedicated simulation strategy. For both the CFD simulations, the governing Navier-Stokes equations were solved in ANSYS Fluent by applying a finite volume method.

Moving boundary set-up – Firstly, we built the computational grid of the 0% phase, selected as baseline configuration (Figure 2a). The grid, hereafter referred to as source mesh (M_S), was made up of tetrahedral elements with an average edge size of 1 mm and 5 near-wall refining layers of wedge elements with a growth rate of 1.2 and a total thickness of 1.35 mm. Then, we employed an in-house non rigid registration algorithm [19] in single-scale modality to map the M_S wall on the target geometries of each phase of the cardiac cycle. The registration process was performed on open 3D models to exploit the aortic inlet and outlets boundary edges as anatomical constraints (Figure 2b). To preserve the inflation layers and enforce the mesh at the TA caps during the CFD_{MB} open morphed models were closed. To this purpose the node-by-node wall displacement was evaluated for each registered phase with respect to the M_S (Figure 2c) and interpolated in every point of the Euclidean space $\mathbb{R}^3$ using Gaussian RBF. The

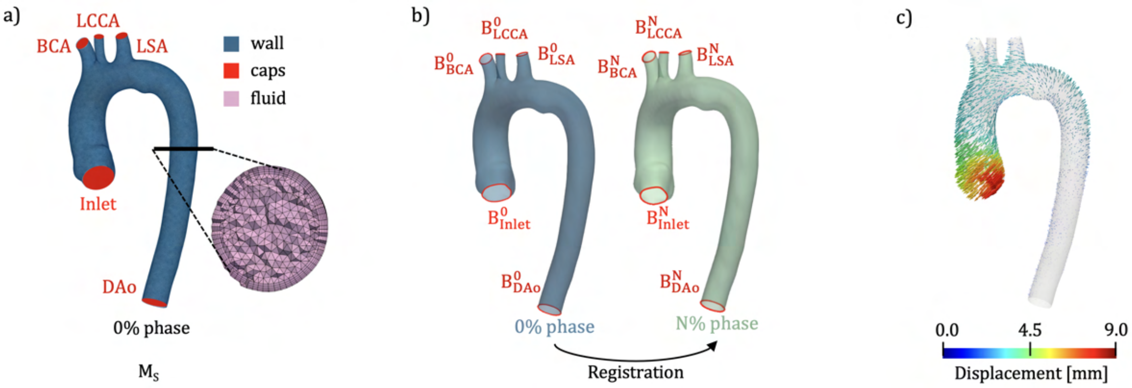

Figure 2: Moving boundary set-up. Computational grid of the baseline configuration (a). Non-rigid registration of the open baseline wall mesh on each N% open target geometry ($N = 5, 10, \ldots, 95\%$). Boundary edges (B) are shown in red (subscript refers to the corresponding cap; superscript refers to the phase) (b). Node-by-node wall displacement field between each N % phase and the baseline wall mesh ($N = 5, 10, \ldots, 95\%$) (c).

so obtained displacement field was applied to the M_S caps. To ensure the coplanarity of points on each cap, we projected nodes onto the plane that best-fitted the corresponding boundary edge. Coordinates of each node of the morphed wall and caps meshes, isotopological to M_S, were extracted for each phase along the x, y, z direction. A low-pass filter in the frequency domain, based on the fast Fourier transform, was implemented to cut high-frequency noise. We employed cubic splines to reconstruct time-continuous nodes trajectories from discrete nodes coordinates associated to each phase of the cardiac cycle. Finally, surface nodes trajectories were prescribed in the CFD_{MB} simulation through an in-house developed user-defined function. The update of volume mesh was handled automatically by the solver on the basis of the new positions of the wall and caps by enabling the dynamic mesh tool.

Numerical simulation – In both the two simulation strategies, blood was assumed as a Newtonian fluid in laminar conditions with a constant viscosity of 0.0035 Pa·s and a density of 1060 Kg/m^3. Figure 3 shows the imposed boundary conditions. Regarding the inlet, we applied a patient-specific flow-velocity. The waveform was obtained computing the systolic volume change of the LV 3D models over time and scaling an idealized diastolic flow to adapt it to the subject stroke volume and cardiac cycle length. A truncated-cone 3D shape was used to mimic the space-distribution of blood velocity in a healthy TAV at the peak systole [15, 20, 21]. We set the ratio between the truncated cone upper area (A_{top}) and lower area (A_{base}) to 0.44 based on the patient-specific aortic valve opening. In terms of outlet boundary conditions pressure was imposed through a lumped 3-element Windkessel model (3EWM).

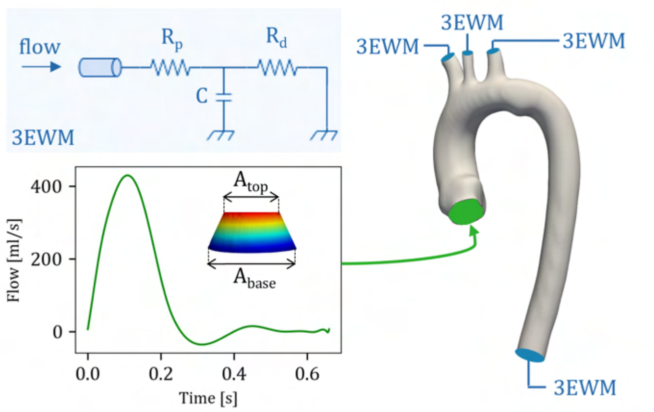

Figure 3: Numerical simulation set-up: inlet and outlet boundary conditions.

A time-step of 0.001 s was used with a maximum of 35 iterations per time-step. Three cardiac cycles were performed and results were evaluated at the last cycle to avoid initial transient effects and obtain converged solutions.

Hemodynamic analysis – For both the performed simulation, results were studied in terms of the velocity magnitude at different cross-sections and times and hemodynamic indices.

The wall shear stress (WSS) evaluation included the time-averaged WSS (TAWSS) and the oscillatory shear index (OSI). The TAWSS represents the average WSS magnitude over the total time of a cardiac cycle (T) and was computed as follows:

$$TAWSS = \frac{1}{T}\int_0^T |WSS(s,t)| \cdot dt \tag{1}$$

The OSI measures changes of direction of the WSS vector from a predominant blood flow direction during the cardiac cycle. It is a dimensionless metric that ranges between 0, when the direction of WSS is consistent during the cardiac cycle, and 0.5, when WSS frequently changes. The OSI was defined according to the following equation:

$$OSI = 0.5\left(1 - \frac{\left|\int_0^T WSS(s,t)\cdot dt\right|}{\int_0^T |WSS(s,t)|\cdot dt}\right) \tag{2}$$

The helical structures of blood flow were measured in terms of the localized normalized helicity (LNH), averaged along the cardiac cycle ($\mathrm{LNH_{avg}}$), which ranges between -1, denoting left-handed rotation and +1, denoting righ-handed rotation. The LNH was defined as the cosine of the angle between the vorticity vector ($\boldsymbol{\omega}$) and the velocity vector ($\mathbf{V}$) as follows:

$$LNH(s,t) = \frac{\mathbf{V}(s,t)\cdot\boldsymbol{\omega}(s,t)}{|\mathbf{V}(s,t)||\boldsymbol{\omega}(s,t)|} \tag{3}$$

For all the hemodynamic indices, results were provided in terms of map distributions; for TAWSS and OSI the median value and interquartile range (IQR) were also evaluated.
Wall stiffness – The TA wall stiffness was evaluated in terms of the pulse wave velocity (PWV), according to the following equation [22]:

$$PWV = \frac{L}{\Delta T_D} \tag{4}$$

where L is the distance along the centerline between the aortic inlet and the DAo outlet cross-sections and ΔT_D is the time delay between flow waveforms at the two TA locations, measured by maximizing the cross-correlation function. Under the assumption of a linear elastic model, given that small deformations occur between the diastolic and the systolic configurations [6], the Young's modulus of the aortic wall (E_W) was evaluated by applying the Moens-Korteweg equation according to [22]:

$$PWV = \sqrt{\frac{E_W\cdot h}{2r\rho}} \tag{5}$$

where h is the wall thickness (set to 2 mm), r is the vessel mean radius and ρ is the blood density.

3 RESULTS

3.1 AI-based image processing

Three-dimensional models of both the TA and the LV were successfully reconstructed for all the phases of the cardiac cycle by means of the multi-label 3D U-Net. Table 1 shows the K-fold cross-validation results of the neural network for the TA and LV segmentation in terms of Dice, precision and recall scores.

3.2 CFD simulations

The $\mathrm{CFD_0}$ and $\mathrm{CFD_{MB}}$ simulations were successfully carried out. The $\mathrm{M_S}$ showed respectively a maximum skewness and an averaged skewness equal to 0.767 and 0.159 that reached peak values of 0.830 and 0.163 along the cardiac cycle in the $\mathrm{CFD_{MB}}$ approach.
Figure 4 shows the comparison between the two performed simulations in terms of the velocity

Table 1: 3D U-Net cross-validation results, computed as mean ± standard deviation, over all folds

	Set	Dice [%]	Precision [%]	Recall [%]
TA	train	97.74 ± 0.09	97.79 ± 0.13	97.70 ± 0.12
	validation	96.01 ± 0.32	96.11 ± 0.89	96.09 ± 1.11
LV	train	97.02 ± 0.07	96.90 ± 0.04	97.18 ± 0.12
	validation	94.98 ± 0.06	94.69 ± 0.42	95.33 ± 1.14

magnitude (v) at different cross-sections on the ascending aorta (S1), aortic arch (S2) and descending aorta (S3). Three time of interest are presented to cope with the velocity distributions at the maximum acceleration time (t_1), the peak systole time (t_2) and the maximum deceleration time (t_3). Significant differences in the velocity patterns were reported at t_1 for the three cross-sections. Regarding velocity peak values the major discrepancy was presented at t_2 in the descending aorta section: the maximum velocity was equal to 0.76 m/s and 1.20 m/s respectively for the CFD_0 and the CFD_{MB} results.

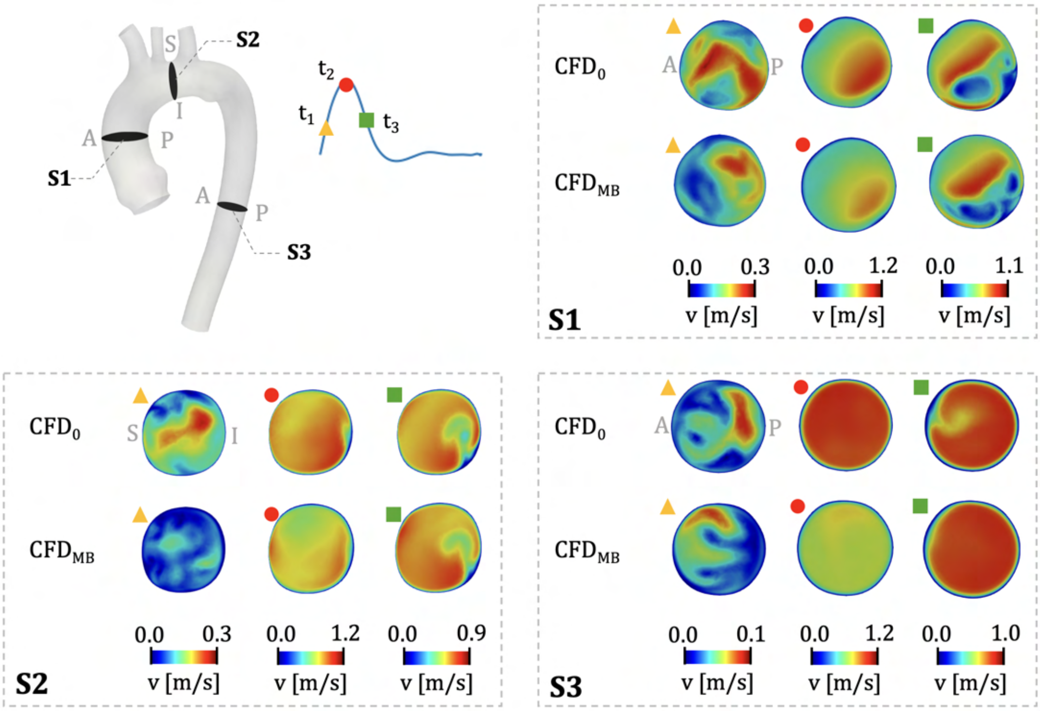

Figure 4: Velocity magnitude for the CFD_0 and CFD_{MB} simulations at specific cross-sections.

Figure 5 shows the time delay between the flow waveform computed at the aortic inlet and the flow waveforms computed at the DAo outlet for the CFD_0 and the CFD_{MB}. As we can observed, in case of CFD_{MB}, the time delay between inlet and DAo outlet flow waveforms was more significant (equal to 0.048 s). By applying Equation 4 between inlet and DAo outlet (L = 0.31 m) the associated PWV value was of 6.44 m/s. Consequently, the Young's modulus resulting from Equation 5 was equal to 0.5 MPa.

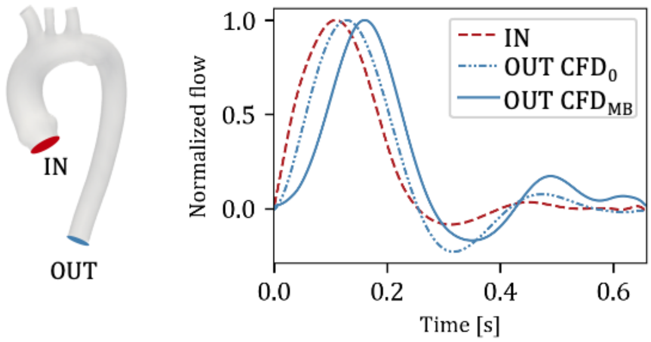

Figure 5: Flow waveforms at the aortic inlet (IN) and descending aorta outlet (OUT).

The TAWSS, OSI and LNH distributions are shown in Figure 6 for the two performed simulation strategies. The differences in TAWSS patterns were more pronounced in the ascending aorta. However, discrepancies in TAWSS values were found in the entire TA. The CFD_{MB} approach resulted in an overall median TAWSS which was 16.87 % lower with respect to the CFD_0. The median TAWSS was of 1.66 Pa (IQR = 1.51 – 2.07 Pa) for the CFD_{MB} and of 1.94 Pa (IQR = 1.73 – 2.33 Pa) for the CFD_0. For both the simulation strategies the WSS presented inconsistent directions over the cardiac cycle mainly in the aortic root, at the supra-aortic bifurcations and in the distal descending aorta. The CFD_{MB} showed an increase of the median OSI of 4.16 %, compared to the CFD_0. The CFD_{MB} an the CFD_0 showed median values respectively of 0.25 (IQR = 0.16 – 0.35) and of 0.24 (IQR = 0.15 – 0.33).
Regarding the helicity analysis, both the approaches highlighted counter rotating flows, with balanced right-handed and left-handed structures. Neverthless, consistent differences in the LNH_{avg} profiles at different cross-sections were highlighted in the CFD_{MB}, compared to the CFD_0 simulation.

4 DISCUSSION AND CONCLUSIONS

In computational studies of the TA, commonly, CFD simulations assume rigid walls. This hypothesis speeds up the numerical approach, but neglects how wall motion affects the flow. Instead, FSI simulations compute the interaction between the compliant aorta and blood, but they demand high computational times and mechanical information on the vessel wall that introduces uncertainties in the method. Given that TA undergoes large deformations due to LV function, the effects of aortic geometrical change on hemodynamics are recognized to be non-negligible [23]. Moreover, usually, CFD approaches impose literature-derived boundary conditions, affecting the patient-specific feature of methods.
In this study we developed and implemented a new approach to set-up accurate and patient-specific moving boundary CFD simulations, based on a mesh morphing technique. The presented method, starting from 4D CT scans, modelled the geometrical variations of the entire TA throughout the cardiac cycle and allowed the setting of patient-specific inflow conditions as

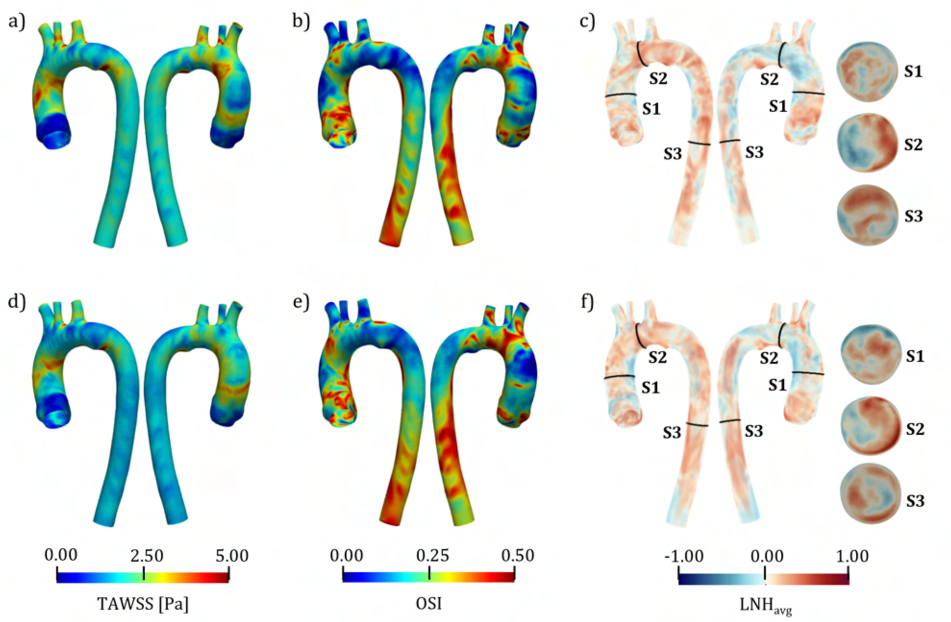

Figure 6: Hemodynamic results in terms of TAWSS, OSI and LNH_{avg} obtained from the two performed simulation strategies: CFD_0 (a-c) and CFD_{MB} (d-f). Distribution maps are shown in the front and back views. The LNH_{avg} is plotted as volume maps and at specific cross-sections (S1, S2, S3).

LV volume changes. Computational times are comparable (1.3x) to those of the rigid wall simulation. The embedding of in-vivo measurements in terms of wall displacement and flow waveform can represent a significant step to overcome the limitation of the state-of-the-art methods.
The comparison of CFD_0 and CFD_{MB} hemodynamics highlights significant differences in terms of velocities, WSS-based indices and helicity parameters. Thus, the geometrical variation of the vessel during the cardiac cycle represents a determinant in the assessment of the TA hemodynamics. Finally, the CFD_{MB} simulation results able to compute the time delay which occurs between the flow waveform along the vessel lumen. This delay, which is an effect of the wall compliance, can not be captured by the rigid-wall approach and allows an estimation of the TA stiffness [24].

REFERENCES

[1] Catapano, F., Pambianchi, G., Cundari, G., Rebelo, J., Cilia, F., Carbone, I., Catalano, C., Francone, M., and Galea, N.. 2020. 4D flow imaging of the thoracic aorta: is there an added clinical value? Cardiovasc Diagn Ther 10, no. 4. https://doi.org/10.21037/cdt-20-452

[2] Zhuang, B., Sirajuddin, A., Zhao, S., and Lu, M. 2021. The role of 4D flow MRI for clinical applications in cardiovascular disease: current status and future perspectives. Quant Imaging Med Surg 11, no. 9, 4193–4210. https://doi.org/10.21037/qims-20-1234

[3] Humphrey, J. D., and Schwartz, M. A. 2021. Vascular Mechanobiology: Homeostasis, Adaptation, and Disease. Annu Rev Biomed Eng 23, 1–27. https://doi.org/10.1146/annurev-bioeng-092419-060810

[4] Ong, C. W., Wee, I., Syn, N., Ng, S., Leo, H. L., Richards, A. M., and Choong, A. M. T. L. 2020. Computational Fluid Dynamics Modeling of Hemodynamic Parameters in the Human Diseased Aorta: A Systematic Review. Ann Vasc Surf 63, 336–381. https://doi.org/10.1016/j.avsg.2019.04.032

[5] Pons, R., Guala, A., Rodríguez-Palomares, J. F., Cajas, J. C., Dux-Santoy, L., Teixidó-Tura, G., Molins, J. J., Vázquez, M., Evangelista, A., and Martorell, J. 2020. Fluid-structure interaction simulations outperform computational fluid dynamics in the description of thoracic aorta haemodynamics and in the differentiation of progressive dilation in Marfan syndrome patients. R Soc Open Sci 7, no. 2. https://doi.org/10.1098/rsos.191752

[6] Vignali, E., Gasparotti, E., Celi, S., and Avril, S. 2021. Fully-Coupled FSI Computational Analyses in the Ascending Thoracic Aorta Using Patient-Specific Conditions and Anisotropic Material Properties. Front Physiol 12, 732561. https://doi.org/10.3389/fphys.2021.732561

[7] Celi, S., Gasparotti, E., Capellini, K., Bardi, F., Scarpolini, M. A., Cavaliere, C., Cademartiri, F., Vignali, E. 2023. An image-based approach for the estimation of arterial local stiffness in vivo. Front Bioeng Biotechnol 11, https://doi.org/10.3389/fbioe.2023.1096196

[8] Nair, P.J., Pfaller, M.R., Dual, S.A. Loecher, M., McElhinney, D.B, Ennis, D.B., and Marsden, A.L. 2023. Hemodynamics in Patients with Aortic Coarctation: A Comparison of in vivo 4D-Flow MRI and FSI Simulation. In Functional Imaging and Modeling of the Heart, edited by : Bernard, O., Clarysse, P., Duchateau, N., Ohayon, J., Viallon, M. FIMH 2023. Lecture Notes in Computer Science, 13958. Springer, Cham. https://doi.org/10.1007/978-3-031-35302-4_53

[9] Zhu, W., Wang, Y., Chen, Y., Liu, J., Zhou, C., Shi, Q., Huang, S., Yang, C., Li, T., and Xiong, B. 2022. Dynamic Changes in the Aorta During the Cardiac Cycle Analyzed by ECG-Gated Computed Tomography. Front Cardiovasc Med 9, 793722. https://doi.org/10.3389/fcvm.2022.793722

[10] Capellini, K., Vignali, E., Costa, E., Gasparotti, E., Biancolini, M. E., Landini, L., Positano, V., and Celi, S. (2018). Computational Fluid Dynamic Study for aTAA Hemodynamics: An Integrated Image-Based and Radial Basis Functions Mesh Morphing Approach. J Biomech Eng, 140, no. 11, 111007. https://doi.org/10.1115/1.4040940

[11] Capellini, K., Gasparotti, E., Cella, U., Costa, E., Fanni, B. M., Groth, C., Porziani, S., Biancolini, M. E., and Celi, S. 2021. A novel formulation for the study of the ascending aortic fluid dynamics with in vivo data. Med Eng Phys 91, 68–78. https://doi.org/10.1016/j.medengphy.2020.09.005

[12] Calò, K., Capellini, K., De Nisco, G., Mazzi, V., Gasparotti, E., Gallo, D., Celi, S., and Morbiducci, U. 2023. Impact of wall displacements on the large-scale flow coherence in ascending aorta. J Biomech 154. https://doi.org/10.1016/j.jbiomech.2023.111620

[13] Youssefi, P., Gomez, A., Arthurs, C., Sharma, R., Jahangiri, M., and Alberto Figueroa, C. 2018. Impact of Patient-Specific Inflow Velocity Profile on Hemodynamics of the Thoracic Aorta. Jo Biomech Eng 140, no. 1. https://doi.org/10.1115/1.4037857

[14] Mariotti, A., Boccadifuoco, A., Celi, S., and Salvetti, M.V. 2021. Hemodynamics and stresses in numerical simulations of the thoracic aorta: Stochastic sensitivity analysis to inlet flow-rate waveform. Comput. Fluids 230, 105123. doi:10.1016/j.compfluid.2021.105123

[15] Mariotti, A., Celi, S., Antonuccio, M. N., and Salvetti, M.V. 2023. Impact of the Spatial Velocity Inlet Distribution on the Hemodynamics of the Thoracic Aorta. Cardiovasc Eng Technol 14, no.5 , 713–725. https://doi.org/10.1007/s13239-023-00682-2

[16] Ramaekers, M. J. F. G., van der Vlugt, I. B., Westenberg, J. J. M., Perinajová, R., Lamb, H. J., Wildberger, J. E., Kenjereš, S., and Schalla, S. (2024). Flow patterns in ascending aortic aneurysms: Determining the role of hypertension using phase contrast magnetic resonance and computational fluid dynamics. Comput Biol Med, 172, 108310. https://doi.org/10.1016/j.compbiomed.2024.108310

[17] Li, Z., Mao, W. 2023. A fast approach to estimating Windkessel model parameters for patient-specific multi-scale CFD simulations of aortic flow. Comput Fluids 259, 105894. https://doi.org/10.1016/j.compfluid.2023.105894

[18] Isensee, F., Jaeger, P.F., Kohl, S.A.A., and Maier-Hein, K.H. 2021. nnU-Net: a self-configuring method for deep learning-based biomedical image segmentation. Nat Methods 18, 203–211. https://doi.org/10.1038/s41592-020-01008-z

[19] Scarpolini, M.A., Mazzoli, M., and Celi, S. 2023. Enabling supra-aortic vessels inclusion in statistical shape models of the aorta: a novel non-rigid registration method. Front Physiol 14, 1211461. https://doi.org/10.3389/fphys.2023.1211461

[20] Antonuccio, M.N., Mariotti, A., Celi, S., and Salvetti, M.V. 2020. Effects of the Distribution in Space of the Velocity-Inlet Condition in Hemodynamic Simulations of the Thoracic Aorta. In Bioinformatics and Biomedical Engineering, edited by Rojas, I., Valenzuela, O., Rojas, F., Herrera, L., and Ortuño, F. IWBBIO 2020. 63-74. https://doi.org/10.1007/978-3-030-45385-5_6

[21] Youssefi, P., Gomez, A., He, T., Anderson, L., Bunce, N., Sharma, R., Figueroa, C. A., and Jahangiri, M. 2017. Patient-specific computational fluid dynamics-assessment of aortic hemodynamics in a spectrum of aortic valve pathologies. J Thorac Cardiovasc Surg 153, no.1, 8–20. https://doi.org/10.1016/j.jtcvs.2016.09.040

[22] Houriez-Gombaud-Saintonge, S., Mousseaux, E., Bargiotas, I., De Cesare, A., Dietenbeck, T., Bouaou, K., Redheuil, A., Soulat, G., Giron, A., Gencer, U., Craiem, D., Messas, E., Bollache, E., Chenoune, Y., and Kachenoura, N. 2019. Comparison of different methods for the estimation of aortic pulse wave velocity from 4D flow cardiovascular magnetic resonance. J Cardiovasc Magn Reson 21, no. 1, 75. https://doi.org/10.1186/s12968-019-0584-x

[23] Reymond, P., Crosetto, P., Deparis, S., Quarteroni, A., and Stergiopulos, N. 2013. Physiological simulation of blood flow in the aorta: comparison of hemodynamic indices as predicted by 3-D FSI, 3-D rigid wall and 1-D models. Med Eng Phys 35, no. 6, 784–791. https://doi.org/10.1016/j.medengphy.2012.08.009

[24] Boccadifuoco, A., Mariotti, A., Capellini, K., Celi, S., and Salvetti, M. V. 2018. Validation of Numerical Simulations of Thoracic Aorta Hemodynamics: Comparison with In Vivo Measurements and Stochastic Sensitivity Analysis. Cardiovas Eng Technol 9, no. 4, 688–706. https://doi.org/10.1007/s13239-018-00387-x